JOURNAL OF COLLOID AND INTERFACE SCIENCE 207, 119–127 (1998)
ARTICLE NO. CS985761

Observation of Oriented Close-Packed Lattice Planes in Polycrystalline Hard-Sphere Solids

Andreas Heymann, Andreas Stipp, Christian Sinn,[1] and Thomas Palberg

Institut für Physik der Johannes-Gutenberg-Universität, Staudingerweg 7, 55099 Mainz, Germany

E-mail: Christian.Sinn@uni-mainz.de

Received March 23, 1998; accepted July 14, 1998

We report time-resolved Bragg scattering experiments on solidifying colloidal suspensions of hard spheres. The polar angle-averaged, integrated intensity of the (111) and (311) reflections show a transient, two-step behavior below melting, which depends in a complex way on the volume fraction and is not present for (200) or (220). Detailed analysis of the full two-dimensional scattering pattern reveals intensity maxima of sixfold symmetry close to the position of the (111) and (311) Debye–Scherrer rings. These can be explained assuming oriented crystals with close-packed planes parallel to the container walls. We show that the observed temporal behavior is due to competing homogeneous and heterogeneous nucleation and growth scenarios. © 1998 Academic Press

Key Words: **crystallization; colloids; hard spheres; light scattering.**

INTRODUCTION

Throughout the last decade polymer-coated colloidal spheres in organic solvents were shown to resemble very closely the behavior of hard spheres (1, 2), which are a comprehensively studied model both in experimental and theoretical work and computer simulations. Investigations comprise a large variety of fundamental condensed matter problems, ranging from diffusional dynamics over transport properties to phase behavior. In general, very good agreement of theory and experimental data is observed. Even inevitable technical complications, like particle polydispersity and particle swelling in an organic solvent (3), may be included in the analysis. Since temperature is not a relevant thermodynamic parameter for a hard-sphere system, the equation of state depends only on the particle concentration in the solvent, which is conveniently expressed in terms of its volume fraction ϕ (4, 5). Below the freezing volume fraction $\phi_f = 0.494$, the equilibrium structure is fluid. Between $\phi_f < \phi < \phi_m$ the fraction of close-packed crystals increases with ϕ. Above the melting volume fraction $\phi_m = 0.545$ the sample solidifies completely at the density of the former shear-melt (6). Under normal gravity a kinetic glass transition is reported (1, 7, 8) to appear at $\phi_g \approx 0.58$.

[1] To whom correspondence should be addressed.

Due to the colloid-specific time and length scales the kinetics of crystal nucleation and growth is conveniently accessible with optical methods, where microscopy and light scattering yield complementary information from real and reciprocal space (9, 10).

Both small-angle light scattering experiments (11–13) to investigate the solidification at the level of individual crystallites and Bragg scattering experiments (12, 14, 15) have been reported. Experimental work is supported by theory and computer modeling (16). The results are interpreted either in terms of kinetic exponents (11, 13) or of classical theories of nucleation and growth (11, 14, 15). Both are severely complicated by a pronounced transient behavior (16), while the underlying microscopic mechanisms of nucleation, growth, and ripening are not always identified to a sufficient extent.

We therefore perform time-resolved Bragg intensity measurements on shear-molten samples of various volume fractions ϕ. The polar angle-averaged data unexpectedly show qualitatively different temporal behavior for different reflections (hkl). In addition, at early times we observe the appearance of distinct sixfold symmetric reflections in the two-dimensional scattering patterns, while at later times the expected Debye–Scherrer rings of the polycrystalline sample dominate. We interpret these findings in terms of an early appearance of close-packed layers oriented parallel to the container walls, while for later times the formation of polycrystalline material via homogeneous nucleation dominates.

The description of the employed materials and techniques given in the next section will be followed by an explanation of our observations from crystallographic considerations. In conclusion, we discuss our data in view of results from other authors.

MATERIALS AND METHODS

The colloidal particles investigated in this study are polymer-coated PMMA spheres (17), kindly provided by W. van Megen and S. M. Underwood. The core radius of 435 nm and a polydispersity of 2.5% were determined from static form factor measurements under contrast variation with

0021-9797/98 $25.00
Copyright © 1998 by Academic Press
All rights of reproduction in any form reserved.

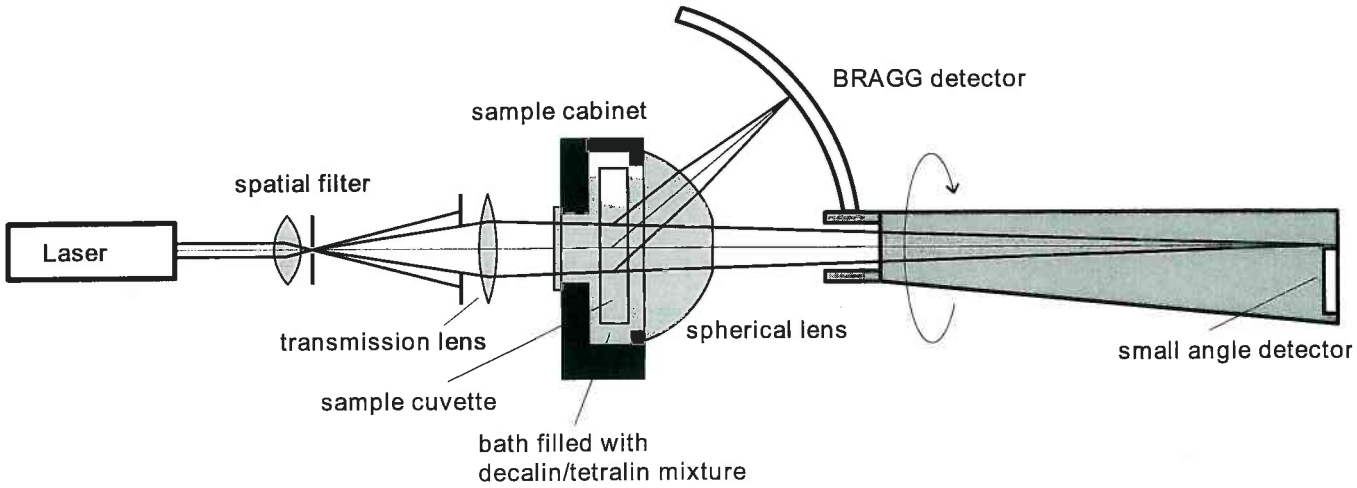

FIG. 1. Optical setup of the crystallization experiment. Note that sample, index matching bath, and spherical lens all have the same refractive index.

correction for multiple scattering (18); sedimentation measurements as performed by Paulin and Ackerson (19) yield the effective hard-sphere volume fraction ϕ of the samples; the lattice constants were determined from the Bragg scattering data. Combined evaluation yields a hard-sphere radius of $R = 445$ nm corresponding to a 10 nm PHSA coating thickness.

In order to obtain nearly perfect index matching, the particles are suspended in a decalin/tetralin mixture, thermostated to 0.1 K. However, inevitably the particle scattering cross section is not zero, because the polymer coating and the PMMA core differ in refractive index and the polymer core appears to be swollen selectively by tetralin (18). No influences of ambient temperature fluctuations on the form factor were detected. Different ϕ were obtained by diluting a sample of known concentration while maintaining the refractive index match. Careful sealing minimizes evaporation. Uncertainties in sample concentrations were well below 1% and trace back to the uncertainties of the phase boundaries given in literature. The suspensions were shear-molten prior to the measurements by slowly tumbling the rectangular glass cuvettes with an optical path length of 5 mm through an axis parallel to the laser beam in the scattering experiment. Stopping the tumbling and inserting the sample into the light scattering apparatus defines $t = 0$ min.

The optical setup, which is shown in Fig. 1, has been designed to simultaneously record small angle and Bragg scattering data; we here concentrate on the latter one. The beam of a HeNe laser ($\lambda = 632.8$ nm) is expanded to a beam diameter of 8 mm and illuminates the crystallizing sample, which is hold in a bath having the same refractive index ($n \approx 1.5$) as the sample. A spherical lens with again the same refractive index collects the light scattered in the sample under equal angles into a common focal point; the optical imaging is equivalent to that of one refracting spherical surface separating the scattering medium and air. Bragg reflections as a function of scattering angle θ are projected on photodiode arrays mounted to a frame which is rotated about the optical (polar) axis during one measurement. This allows to either record the complete two-dimensional scattering pattern $I(\theta, \varphi)$, which is exploited in this contribution for the first time, or to perform an angular average over the polar angle φ to yield $\bar{I}(\theta)$ (12). As the rotation period of the detector arm is small compared to the time scales of crystallization, the temporal evolution of the scattering pattern $I(\theta, \varphi; t)$ or $\bar{I}(\theta; t)$ is obtained from successive measurements.

RESULTS AND DISCUSSION

Crystal Structure

From previous work it is known that hard-sphere crystals adopt a close-packed structure. For atomic systems, the interaction potential range extends well beyond the nearest neighbor distance, thus favoring packing of hexagonal planes in either of the two extreme stacking modes, fcc (ABCABC . . .) or hcp (ABABAB . . .). Since hard spheres are intuitively expected to exhibit only interactions with nearest neighbors, a complete random stacking of close-packed hexagonal layers would be the expected crystal structure. However, already very early simulations show that also next-nearest neighbors contribute to the interaction potential (6). These results are confirmed by very recent computer simulations (20, 21), where also a tiny preference for fcc crystals over hcp is reported.

The degree of stacking disorder in the system is customary quantified by a stacking probability α, which describes the probability of finding a third plane nonidentical to the first one, i.e. $\alpha = 0$, 0.5, or 1 for hcp, complete random stacking, and fcc, respectively. Experimental observations give no consistent picture up to now. While Pusey *et al.* (22)

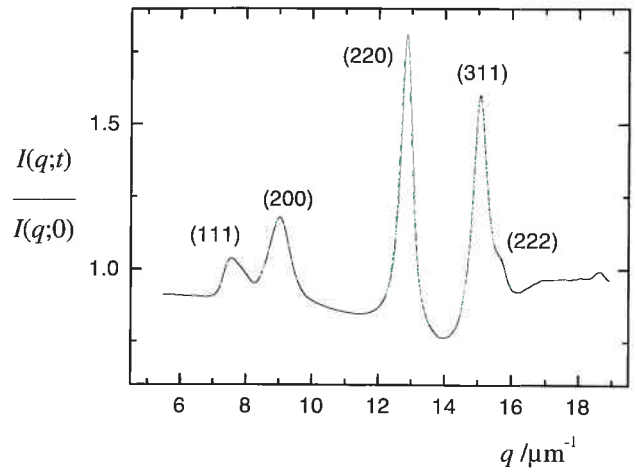

FIG. 2. Normalized Bragg scattering intensity of a sample with ϕ = 0.545, observed after t = 100 min after cessation of the shear-flow. Miller indices (fcc) are indicated.

report a complete random stacking (α = 0.5) for homogeneous nucleated crystals, they observe a larger α in the compacted sediment. Similarly, Elliot *et al.* (23) obtain by direct microscopic observation of the crystal packing α = 0.60 ± 0.07, a value which seems to increase with time. Coated PMMA spheres (similar to those in the present contribution) were used for these investigations. A similar observation has been reported by Dux and Versmold (24) employing charge-stabilized polystyrene sphere suspensions of very low ionic strength. They report fcc crystals with α = 0.55, which increases with time to almost α = 0.75. On the other hand, Verhaegh *et al.* (25) investigate the crystallization of suspensions of coated silica spheres. They determine α = 0.4 ± 0.2. In a long-time settled sample they even find an hcp crystal structure.

The crystalline structure in our experiments may be read from $\bar{I}(q;\ t = 100\ \text{min})$, which is shown in Fig. 2 for a sample at ϕ_m = 0.545; the scattering vector is $q = 4\pi n/\lambda \sin(\theta/2)$. Miller indices in this contribution will in general follow fcc indexing if not otherwise noted. Five different Bragg peaks are clearly resolved. Common to fcc and hcp lattices are the (111), (220), (311), and (222) reflections. The first pronounced minimum of the particle form factor almost coincides with (111), which consequently shows only a small intensity and even becomes invisible for some samples. The second minimum is located at scattering angles slightly above (222). The (200), found only in fcc lattices, is broadened due to stacking faults. From the mere existence of (200) we conclude $\alpha > 0.7$ (26); during solidification and ripening we find α even to increase to $\alpha \approx 0.9$ (18).

Angular Averaged Results

The data shown in Fig. 2 have been normalized according to $\bar{\imath}(q;\ t) = \bar{I}(q;\ t = 100\ \text{min})/\bar{I}(q;\ t = 0\ \text{min})$. This corrects for differences in the detectors and for the particle form factor, which we did not calculate, because the optical parameters of the particles are not known to a sufficient accuracy. $\bar{\imath}(q;\ t)$ can be written as

$$\bar{\imath}(q;\ t) = \frac{\bar{I}(q;\ t)}{\bar{I}(q;\ 0)} = \frac{S_B(q;\ t) + S_{diff}(q;\ t)}{S_{fluid}(q;\ 0)} = \frac{S_B(q;\ t)}{S_{fluid}(q;\ 0)} + B(q;\ t), \quad [1]$$

where $S_B(q;\ t)$ describes the contributions due to the Bragg reflections, $S_{fluid}(q;\ t)$ describes the fluid phase at t = 0, and $S_{diff}(q;\ t)$ describes those contributions stemming from diffusive scattering due to random stacking or grain boundaries as well as the contributions of the time-dependent fluid fraction. We assume that the baseline $B(q;\ t)$ changes sufficiently slowly and continuously, and that $S_{fluid}(q;\ 0)$ does not lead to considerable distortions of a reflection. It is then possible to construct a straight baseline and to isolate the reflection's time dependence for further quantitative analysis. We note, however, that the fluid structure factor maximum for our system is located close to the position of (111), thus invalidating the above mentioned assumptions for the evaluation of the (111) data.

As a measure of the solidification kinetics we therefore use the temporal evolution of the integrated intensity $\bar{\imath}_{peak}(t) = \int_{\Delta q_{peak}} \bar{\imath}(q;\ t)dq \sim NV$ for (311) and (220); N is the number of crystals, and V is a mean volume of one crystal. Eight samples with different ϕ are shown in Fig. 3. In general, we observe a continuous increase in intensity with time, corresponding to an increase in crystallized fraction, reaching a plateau value. We interpret this finding as a transition from a growth period (increasing NV) to ripening (NV = constant). Due to an increase in both nucleation and growth rate, the crystallization kinetics accelerates with increasing particle concentration, i.e. crystal appearance and completion of crystallization occur at ever earlier times. We leave the detailed discussion of the homogeneous nucleation, growth, and ripening results to a forthcoming publication.

There is, however, a pronounced difference in the temporal behavior of (311) and (220). The former clearly exhibits two processes with different growth exponents: a slower one (of low growth exponent), which is absent in (220) and leads to an appreciable Bragg scattered intensity in (311) even when there is no intensity in (220), and a faster one (of high growth exponent), which is comparable in slope to the kinetics visible in (220). Appearance of intensity in (220) approximately coincides with the transition to the second process in (311). The slower component loses importance with increasing concentration and disappears above ϕ_m. We note that (111) behaves qualitatively similar to (311), while the two-step behavior is absent for (200).

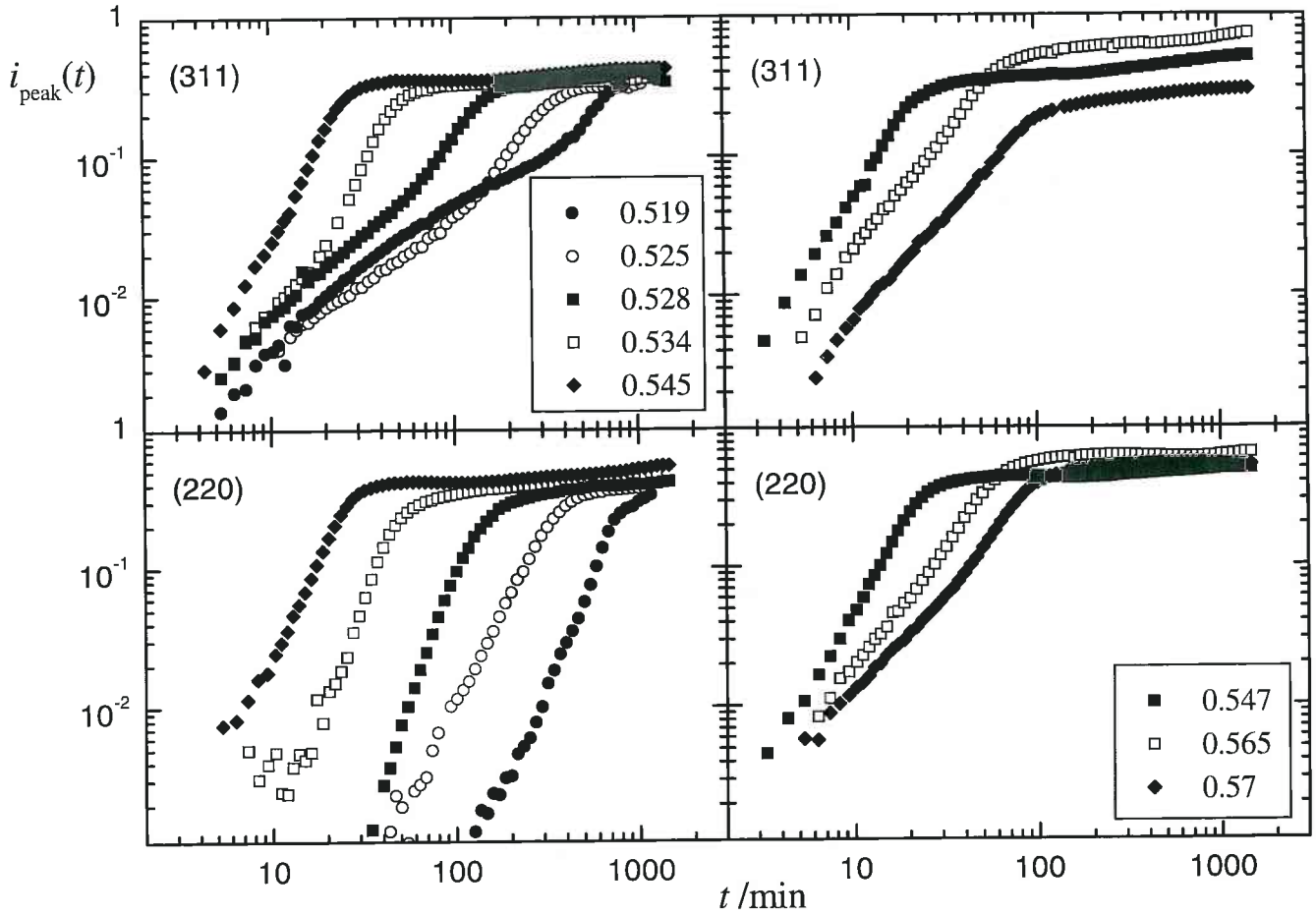

FIG. 3. Integrated intensity of the (311) and the (220) Bragg peak, as a function of time after cessation of the shear flow. The volume fraction, as indicated in the corresponding inset, increases from the right to the left for data below ϕ_m and in opposite direction for data taken above ϕ_m.

A similar observation was reported by Harland *et al.* (15), who found two-step behavior well above ϕ_m. In their case the contribution of the slower component increased with increasing ϕ which is opposed to the trend seen in our data at $\phi < \phi_m$. A careful inspection of our data at high ϕ shows that in our systems the scenario observed by Harland *et al.* is not visible to a significant extent (cf. Fig. 3).

Two-Dimensional Scattering Patterns

In further pursuit of our observation we analyzed the Bragg scattering data prior to the rotational averaging process. Figure 4a shows a polar plot $i(\theta, \varphi; t = 31$ min) of the most diluted sample ($\phi = 0.525$). The angular resolution in φ direction is 360/32 = 11.25°. (111) and (311) of homogeneously nucleated crystals are visible as very faint Debye–Scherrer rings. Seemingly superimposed to these, both show a distinct sixfold intensity pattern with (111) twisted by 30° with respect to (311). After $t = 100$ min (Fig. 4b), the Debye–Scherrer rings have gained intensity. (220) is now visible as a third ring, which shows no comparable sixfold intensity pattern. (200) is still not visible at this time. The overall increased contrast is due to the decrease in fluid volume fraction, concentrating the scattered intensity into the Bragg reflections; the dark ring close to (111) is due to a nonconstant baseline (cf. Eq. [1]).

We next will explain these unexpected sixfold scattering patterns as due to heterogeneously nucleated close-packed planes, oriented perpendicular to the incident laser beam, i.e. parallel to the cuvette walls. To do so, let us recall some elementary, but nonetheless tricky, crystallography.

We assume a real-space hcp coordinate system described by the lattice vectors

$$\vec{a} = \frac{\sqrt{3}a_h}{2}\cdot\vec{e}_x + \frac{a_h}{2}\cdot\vec{e}_y, \quad \vec{b} = -\frac{\sqrt{3}a_h}{2}\cdot\vec{e}_x + \frac{a_h}{2}\cdot\vec{e}_y,$$

$$\vec{c} = \sqrt{\frac{8}{3}}\,a_h\cdot\vec{e}_z, \quad [2a]$$

where $\vec{a}$ and $\vec{b}$ are perpendicular and $\vec{c}$ is parallel to the

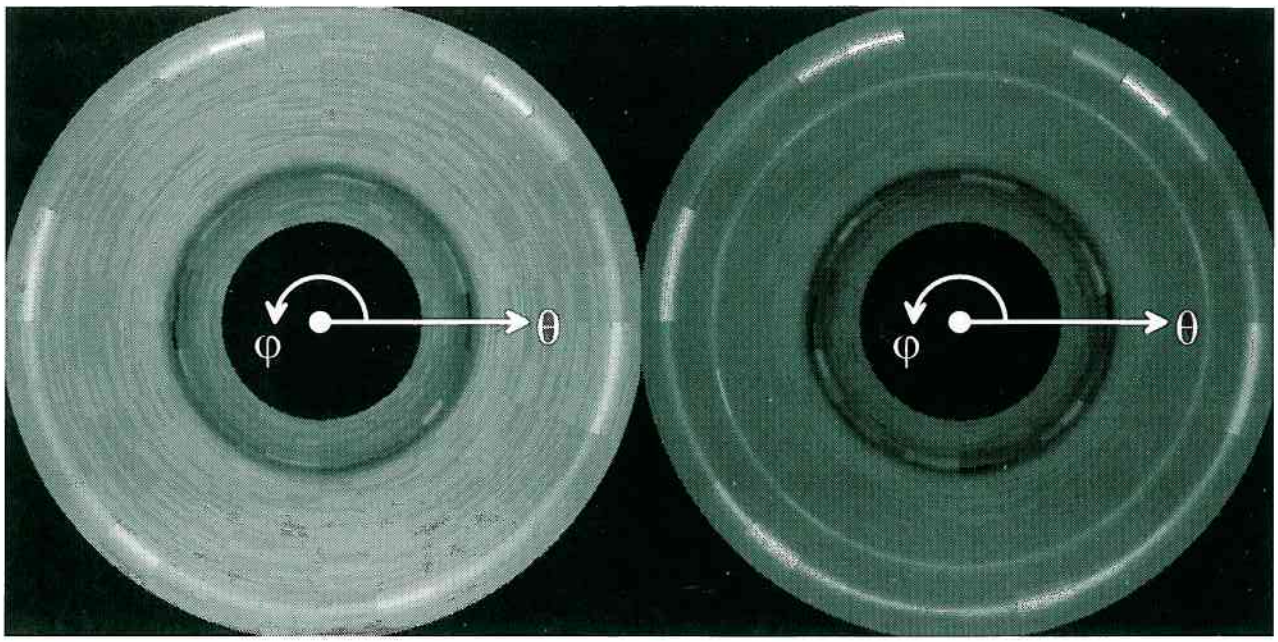

FIG. 4. Polar plot of normalized two-dimensional scattering pattern of a sample with $\phi = 0.525$. Radial axis is the scattering angle θ, transverse axis is the azimuth φ, through which the detector usually is rotated in order to obtain angular averaged data: (a) $t = 31$ min; (b) $t = 100$ min.

stacking direction. a_h is the hexagonal nearest neighbor distance. The corresponding reciprocal lattice vectors are

$$\vec{A} = \frac{2\pi}{\sqrt{3}a_h}\cdot\vec{e}_x + \frac{2\pi}{a_h}\cdot\vec{e}_y, \quad \vec{B} = -\frac{2\pi}{\sqrt{3}a_h}\cdot\vec{e}_x + \frac{2\pi}{a_h}\cdot\vec{e}_y,$$

$$\vec{C} = \frac{2\pi\sqrt{3}}{\sqrt{8}a_h}\cdot\vec{e}_z. \quad [2b]$$

If we split the arbitrary reciprocal lattice vector $\vec{G}_{hkl} = h\vec{A} + k\vec{B} + l\vec{C}$ into components perpendicular and parallel to the stacking direction $[001]_{hcp}$, $\vec{G}_\perp$ and $\vec{G}_\parallel$, respectively, and normalize by $2\pi/a_c$ for future convenience, where $a_c = \sqrt{2}a_h$ is the related cubic lattice constant, we obtain in hexagonal notation:

$$\frac{|\vec{G}_\perp|}{2\pi/a_c} = \sqrt{\frac{8}{3}(h_h^2 + k_h^2 + h_h k_h)}, \quad \frac{|\vec{G}_\parallel|}{2\pi/a_c} = \sqrt{\frac{3}{4}}\cdot l_h. \quad [3a]$$

For the cubic system (i.e. fcc), where $[111]_{fcc}$ is the stacking direction, we obtain

$$\frac{|\vec{G}_\perp|}{2\pi/a_c} = \sqrt{(h_c^2 + k_c^2 + l_c^2) - 1/3(h_c + k_c + l_c)^2},$$

$$\frac{|\vec{G}_\parallel|}{2\pi/a_c} = \frac{h_c + k_c + l_c}{\sqrt{3}}. \quad [3b]$$

Figure 5 presents a corresponding diagram, showing $|\vec{G}_\parallel|$ into the stacking direction on one axis and the *two* perpendicular directions (including an angle of 60°) indicated as $|\vec{G}_\perp|$ on the other axis. Only reciprocal lattice points (hkl) not extinguished in either pure hcp and fcc lattices are shown. The corresponding conditions are

$$\text{hcp: } [(h_h - k_h) = 3n \text{ and } l \text{ even}] \text{ or } [(h_h - k_h) = 3n \pm 1], \quad [4a]$$

$$\text{fcc: } h_c k_c l_c, \text{ all three coefficients even or odd.} \quad [4b]$$

Miller indices are given above and below the symbols for hcp and fcc crystals, respectively.

Starting with a single two-dimensional plane in real space, an array of infinitely extended rods would be present in reciprocal space. An intersection of this array perpendicular to the stacking direction is shown on the left-hand side of Fig. 5. Please note the respective orientation of the six reflections, which are shown in the diagram as corresponding symbols. Proceeding to several planes, the $(00l)_{hcp}$ and $(11l)_{hcp}$ rods shrink to sharp points irrespective of the stacking sequence for every even l. This is due to the fact that the respective reflections are present for hcp as well as for fcc. On the other hand, the $(10l)_{hcp}$ and $(20l)_{hcp}$ rods become sharp points only for a fault-free stacking sequence, i.e. either hcp or fcc. The location of these sharp points is integer l_h for hcp and $l_c = 2n \pm \frac{2}{3}$ for fcc. The occurrence of stacking faults leads to a nonvanishing intensity all along the l direction, which is indicated as broken horizontal lines in Fig. 5. For details we refer the reader, e.g. to Ref. (26).

If the Bragg condition $\vec{q} = \vec{k}_i - \vec{k}_f = \vec{G}_{hkl}$ is satisfied ($\vec{k}_i$

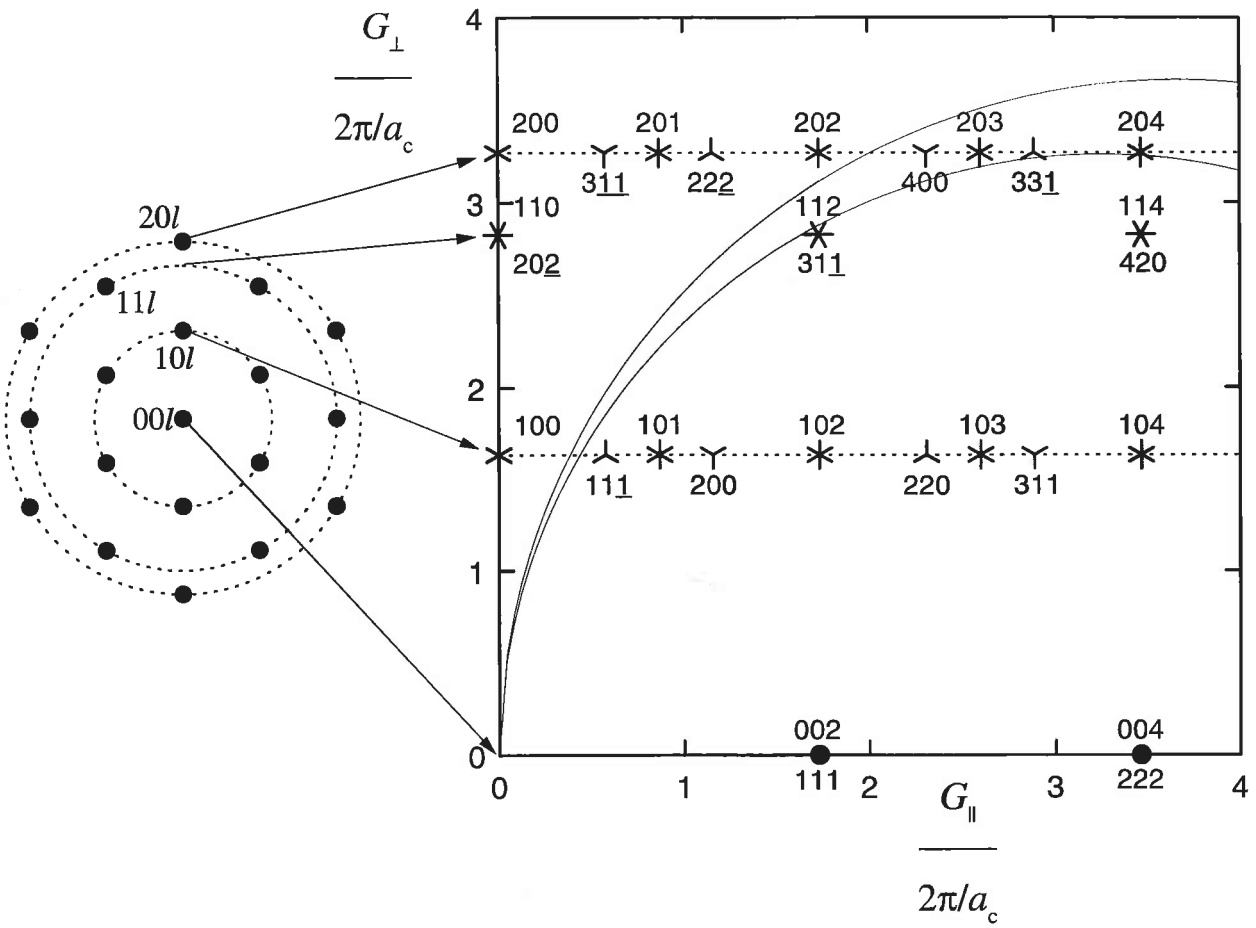

FIG. 5. Ewald construction for close-packed planes with stacking direction parallel to the abscissa. The reciprocal space is put up by a single reciprocal lattice vector parallel ($G_\parallel$) and two vectors perpendicular ($G_\perp$) to the stacking direction, which all have been normalized by the fcc reciprocal lattice constant $2\pi/a_c$. Miller indices for a hexagonal (hcp) or a cubic crystal (fcc) are indicated above and below the symbols, which denote the position of the expected crystal reflections; the expected symmetry of the two-dimensional scattering pattern is also indicated. Two different Ewald spheres are drawn, either for $a_c = 1.4$ μm (our system, lower curve) and for $a_c = 1.5$ μm (upper curve). Random stacking leads to nonvanishing intensity along lines parallel to the abscissa, where either pure hcp or fcc reflections are expected. The corresponding positions are indicated by dotted lines. The points on the left-hand side show an intersection perpendicular to the stacking direction of the array of scattering rods, which would be present for a single close-packed plane.

and $\vec{k}_f$ are the incoming and outgoing wave vectors, respectively), those reflections will be observed which coincide with the Ewald sphere. In Fig. 5, two Ewald spheres are drawn for $\vec{k}_i \| \vec{G}_\parallel$. Their radii are given by $k_{\text{Ewald}}/(2\pi/a_c) = a_c n/\lambda$; for the system investigated in this contribution, $a_c = (16\pi R^3/3\phi)^{1/3} = 1.4$ μm at $\phi = 0.57$ (lower curve in Fig. 5). The orientation of the Ewald sphere is chosen such that the Bragg condition is fulfilled for planes oriented perpendicular to the incident laser beam. For all particles with radius larger than 250 nm, the Ewald sphere crosses the $(10l)_{\text{hcp}}$ line, and a threefold scattering pattern results; the $(20l)_{\text{hcp}}$ line is not observable with our apparatus. We note that only one single stacking fault, thus forming a crystal twin, is necessary to convert the threefold symmetric $\{11\bar{1}\}_{\text{fcc}}$ reflection into a sixfold symmetric one.

In addition, our system's Ewald sphere almost hits the isolated $\{31\bar{1}\}_{\text{fcc}}$. We therefore expect also a sixfold scattering pattern superimposed to the $(311)_{\text{fcc}}$ Debye–Scherrer ring and twisted by 30° with respect to the former six reflections.

Let us sum up the predictions from crystallography. Assuming close-packed planes with their stacking direction parallel to the incident laser beam, we would expect distinct reflections superimposed to the Debye–Scherrer rings. While close to the (111) and the (311) ring sixfold-symmetric reflections, twisted by 30° with respect to each other should be visible, no such pattern is expected close to the (200), (220), or (222) rings. This, however, is exactly what we observe in Fig. 4.

Our experimental observation of the $\{31\bar{1}\}$ planes must be rated as incidental, as several parameters have to be matched to meet the Bragg criterion, namely the refractive index n, the laser wavelength λ, the particle radius R and the lattice constant a (or volume fraction ϕ). Colloidal crystals usually consist of only some ten to some hundreds of lattice planes,

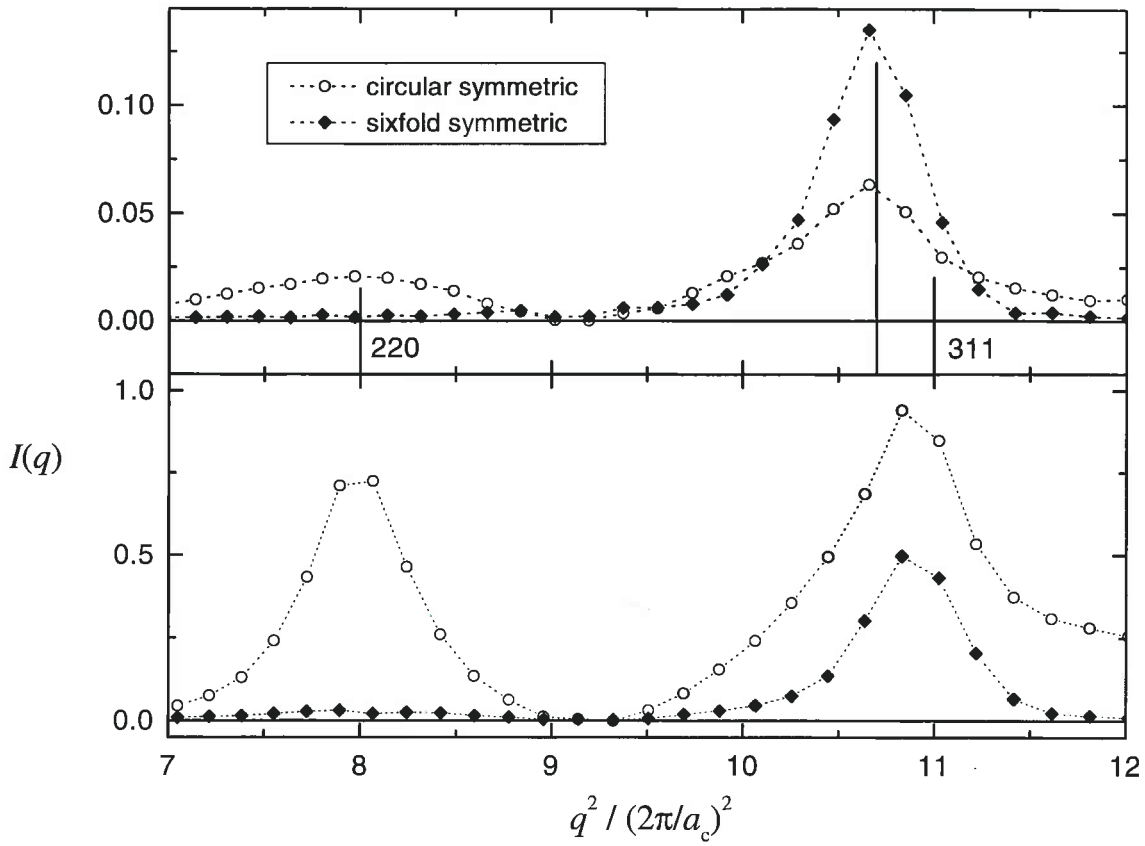

FIG. 6. Normalized intensity of the two-dimensional scattering pattern as a function of q^2, determined on circles with constant q. The data are measures for the respective weight of a sixfold symmetric and a circular symmetric portion. Data were obtained from a sample with $\phi \approx 0.57$ after $t = 20$ min (top) and $t \approx 500$ min (bottom). Expected positions of (220) and (311) are marked. For details see text.

leading to broad Bragg reflections compared to those of atomic systems. It is only this "relaxed" Bragg condition which enables us to observe the $\{31\bar{1}\}$ planes. Indeed, a sample of slightly larger spheres ($R = 500$ nm, upper curve in Fig. 5), where the Ewald sphere does not hit the $\{31\bar{1}\}$ reflections any more, did not show a sixfold pattern superimposed to the (311) Debye–Scherrer ring, while the sixfold pattern close to the (111) Debye–Scherrer ring remained visible.

Shape of the Layered Structure

The angular resolution of our apparatus is large enough to deduce some additional information from the data: For roughly spherical crystallites, small in all three dimensions, a circular Bragg spot of a width determined by those spatial dimensions is expected. In this case, the Ewald construction would predict a Bragg reflection at approximately $qa_c/2\pi = \sqrt{11.2}$. As the Ewald sphere does not hit $\{31\bar{1}\}$ perfectly, the intersection of Ewald sphere and Bragg spot is located above the $(11l)$ line. However, if only a few close-packed layers parallel to the cuvette walls are present which are of considerable lateral extent, an elliptical Bragg spot is expected with some extension in the hexagonal l direction, but thin perpendicular to it. Now, the Ewald construction leads to a Bragg reflection which is located on the $(11l)$ line; the Bragg peak thereby shifts to approximately $qa_c/2\pi = \sqrt{10.7}$.

In Fig. 6 we show data obtained by a Fourier decomposition of the two-dimensional scattering patterns, where the mean intensity and the sixfold periodic intensity has been determined on circles with constant q (i.e. θ). The respective intensities have been determined as a function of the normalized scattering vector $q/(2\pi/a_c)$, where the position of (220) at $qa_c/2\pi = \sqrt{8}$ has been used for the determination of the lattice constant a_c, as it is not influenced by the sixfold reflections. In our analysis we therefore tacitly assume that the lattice constant of the oriented planes is the same as for the bulk crystal. The data shown in Fig. 6 were obtained for a sample with $\phi = 0.57$. This comparatively high volume fraction was chosen because the sixfold reflections remain still visible at long times; the following discussion, however, is valid for lower concentrations, too. Note that the same volume fraction ($\phi = 0.57$) was chosen to draw the Ewald construction of Fig. 5.

At early times ($t = 20$ min), the total scattering is dominated by the sixfold symmetric reflections (cf. Fig. 4). This leads to a very shallow (220) reflection and the observation that

the Debye–Scherrer ring and the sixfold reflections have the same q position. This position, however, is found at approximately $qa_c/2\pi = \sqrt{10.7}$, in accordance with the analysis above. At later times ($t = 500$ min), (220) has gained intensity, which is also true for (311). At the same time, the position of the Debye–Scherrer ring as well as those of the sixfold reflections has shifted to approximately $qa_c/2\pi = \sqrt{11}$. In view of our analysis above we explain this finding with a growth of the oriented layers, thereby converting the elliptical Bragg spot into a smaller circular one.

We note again that Fig. 6 does not imply that the lattice constant is temporally invariant. In fact, we observe an increase from $a_c = 1.34$ μm at $t = 10$ min up to $a_c = 1.37$ μm at $t = 500$ min. This increase is due to a relaxation of the osmotic compression of the crystal present at early times (15); the corresponding data from our investigations will be published in a forthcoming contribution. Notice that this behavior does not explain the shift of the sixfold reflections with time, as both, the Bragg reflection and the Ewald sphere are affected the same way by the increasing lattice constant.

In a very crude manner we can estimate the number of close-packed layers from the position of the sixfold reflections. Let us assume that the Ewald sphere intersects the Bragg spot of a large crystal on the $(11l)$ line, which means that this point is located exactly at $qa_c/2\pi = \sqrt{11}$. The observed initial shift in the position of the sixfold reflections would then be due to their limited extension in stacking direction. Accordingly, the number N of stacked layers can be calculated by assuming an anisotropic Rayleigh–Debye form factor for the crystal with the smallest extension in the stacking direction. From the half-width of the first form factor maximum, $P(qL/2) = \frac{1}{2} \Leftrightarrow qL/2 = 1.8$, we then obtain $\Delta q N a_c/2 = 1.8$, where Δq is the half-width of the Bragg reflection and $N = L/a_c$ is the number of stacked layers in a crystal of thickness L. From Figs. 6 and 5 we obtain $\Delta q a_c/2\pi = \sqrt{11} - \sqrt{10.7} \approx 0.0455$, which leads to $N = 13$. Upon time, the position of the sixfold reflections shifts to larger q, which means that N increases. We note again that N should be taken as an order of magnitude only.

CONCLUDING REMARKS

Let us sum up shortly our results. The observed early temporal behavior of the crystallization kinetics of selected reflections is accompanied by the appearance of heterogeneously nucleated close-packed planes, which are oriented parallel to the container walls.

Accordingly, we explain the different crystallization kinetics observed from the angular averaged data of (311) and (220) (Fig. 3) as follows: At early times close-packed planes form and dominate the integrated Bragg scattering intensity. From its time dependence we deduce these structures to grow. However, when after some induction time the homogeneously nucleated crystals appear, they soon dominate the scattered intensity. As they grow more rapidly, they probably even limit the growth of the plane structures. Accordingly, the (311) data show a superposition of heterogeneous and homogeneous nucleation, whereas the (220) data exhibit only homogeneous nucleation with no influence of heterogeneous nucleation. Above the melting point, the growth of the close-packed planes is inhibited by the large nucleation rate of homogeneous nucleated crystals, which is, even at the highest investigated volume fraction, orders of magnitude larger than at the lowest volume fraction. This observation is in accord with the results from Harland *et al.* (15), with classical nucleation theory and also with data taken from charged spheres (27).

Even in the absence of direct observations, the exactness of the layer orientation parallel to the container walls indicates a large probability of them being very close to the wall. It is tempting, therefore, to explain our observation as the first experimental confirmation of a wetting layer found in computer simulation (28, 29) and theoretical studies (30) of the freezing behavior of hard spheres close to an unstructured wall. This ordered structure then serves as a heterogeneous nucleus for homoepitactic crystal growth. Similar experimental observations of layering-induced nucleation have recently also been reported for Yukawa particles (31).

However, we note that we always observe a single sixfold reflection pattern; as we should be able to observe wall-oriented layers from both walls of the cuvette perpendicular to the laser beam, we at least, even sometimes, expect to observe two sixfold reflections, twisted by a random angle with respect to each other. This might be an indication that the shear-flow used to melt the samples has a long lasting orientational influence on the suspensions. This was already found experimentally by Harland *et al.* (15), who report observations of shear-aligned metastable bulk structures formed during tumbling of the samples, which relax into the fluid structure of the metastable melt which solidifies via homogeneous nucleation. Since their decay is governed by diffusional processes, it is significantly slowed down as the volume fraction is increased and the glass transition is approached. Consequently, a competition between their slow dissipation and the process of homogeneous nucleation results. Above ϕ_g the residues were observed to grow into large irregular crystals (32).

Notice that we observe layers parallel to the container wall (and presumably having their in-plane orientation from formerly applied shear) at volume fractions $\phi \leq \phi_m \ll \phi_g$. In addition, these structures grow in time. Any shear-induced bulk structure should decay rapidly. It is in fact questionable whether metastable bulk structures as described by Harland *et al.* occur at all at low ϕ where diffusional processes are still very rapid.

On the other hand, the typical number of the wall-oriented wetting layers has been reported to be seven (30), which interestingly is of the same order of magnitude as our value.

Since at present we can not unequivocally discriminate experimentally between the described alternatives, identifying

the responsible origin for observing a regular sixfold reflection pattern superimposed to Debye–Scherrer rings remains an interesting challenge.

ACKNOWLEDGMENTS

This work would not exist without the innovative experimental ideas of Klaus Schätzel; his spirit will guide us still longer. Thorough discussions with Bill van Megen are gratefully acknowledged. This work was supported by the Deutsche Forschungsgemeinschaft (Pa 459-6/3) and the MWFZ, Mainz.

REFERENCES

1. Pusey, P. N., and van Megen, W., *Nature (London)* **320,** 340 (1986).
2. Pusey, P. N., *in* "Liquids, Freezing and Glass Transition" (J. P. Hansen, D. Levesque, and J. Zinn-Justin, Eds.), Proceedings of the Les Houches Summer School, p. 666. North-Holland, Amsterdam 1991.
3. Ottewill, R. H., and Livsey, I., *Polymer* **28,** 109 (1987).
4. Carnahan, N. F., and Starling, K. E., *J. Chem. Phys.* **51,** 635 (1969).
5. Young, D. A., and Alder, B. J., *J. Chem. Phys.* **70,** 473 (1979).
6. Hoover, W. G., and Ree, F. H., *J. Chem. Phys.* **49,** 3609 (1968).
7. Bartsch, E., Frenz, V., Möller, S., and Sillescu, H., *Physica A* **201,** 363 (1993).
8. Russel, W. B., Chaikin, P. M., Zhu, J., Meyer, W. V., and Rogers, R., *Langmuir* **13,** 3871 (1997).
9. Ackerson, B. J. (Ed.), *Phase Transitions* **21**(2–4), (1990).
10. Palberg, T., *Curr. Opinion Colloid Interface Sci.* **2,** 607 (1997).
11. Schätzel, K., and Ackerson, B. J., *Phys. Rev. E* **48,** 3766 (1993).
12. Heymann, A., Stipp, A., and Schätzel, K., *Nuovo Cimento* **16D,** 1149 (1994).
13. He, Y., Ackerson, B. J., van Megen, W., Underwood, S. M., and Schätzel, K., *Phys. Rev. E* **54,** 5286 (1996).
14. Dhont, J. K. G., Smits, C., and Lekkerkerker, H. N. W., *J. Colloid Interface Sci.* **152,** 386 (1992).
15. Harland, J. L., and van Megen, W., *Phys. Rev. E* **55,** 3054 (1997).
16. Ackerson, B. J., and Schätzel, K., *Phys. Rev. E* **52,** 6448 (1995).
17. Antl, L., Goodwin, J. W., Hill, R. D., Ottewill, R. H., Owens, S. M., Papworth, S., and Waters, J. A., *Colloids Surf.* **17,** 67 (1986).
18. Heymann, A., Doctoral Thesis, Kiel, Germany, 1997.
19. Paulin, S. E., and Ackerson, B. J., *Phys. Rev. Lett.* **64,** 2663 (1990).
20. Woodcock, L. V., *Nature (London)* **385,** 141 (1997).
21. Bruce, A. D., Wilding, N. B., and Ackland, G. J., *Phys. Rev. Lett.* **79,** 3002 (1997).
22. Pusey, P. N., van Megen, W., Bartlett, P., Ackerson, B. A., Rarity, J. G., and Underwood, S. M., *Phys. Rev. Lett.* **63,** 2753 (1989).
23. Elliot, M. S., Bristol, B. T. F., and Poon, W. C. K., *Physica A* **235,** 216 (1997).
24. Dux, C., and Versmold, H., *Phys. Rev. Lett.* **78,** 1811 (1997).
25. Verhaegh, N. A. M., van Duijneveldt, J. S., van Blaaderen, A., and Lekkerkerker, H. N. W., *J. Chem. Phys.* **102,** 1416 (1995).
26. Loose, W., and Ackerson, B. J., *J. Chem. Phys.* **101,** 7211 (1994).
27. Palberg, T., Mönch, W., Schwarz, J., and Leiderer, P., *J. Chem. Phys.* **102,** 5082 (1995).
28. Courtemanche, D. J., and van Swol, F., *Phys. Rev. Lett.* **69,** 2078 (1992).
29. Courtemanche, D. J., Pasmore, T. A., and van Swol, F., *Mol. Phys.* **80,** 861 (1993).
30. Ohnesorge, R., Löwen, H., and Wagner, H., *Phys. Rev. E* **50,** 4801 (1994).
31. Grier, D. G., and Murray, C. A., *J. Chem. Phys.* **100,** 9088 (1994).
32. van Megen, W., and Underwood, S. M., *Nature (London)* **362,** 616 (1993).